Three-Dimensional Global Hybrid Simulations of Plasma Transport and Energy Conversion During Solar Wind-Magnetosphere Interactions

San Lu[1,2,3] , Jin Guo[1] , Quanming Lu[1,2,3] , Yukang Shu[1] , Junyi Ren[1] , Rongsheng Wang[1,2,3] , and Rajkumar Hajra[1]

[1]School of Earth and Space Sciences, CAS Center for Excellence in Comparative Planetology, CAS Key Laboratory of Geospace Environment, University of Science and Technology of China, Hefei, China, [2]Deep Space Exploration Laboratory, Hefei, China, [3]Collaborative Innovation Center of Astronautical Science and Technology, Harbin, China

Abstract Plasma transport and energy conversion during solar wind-magnetosphere interactions under northward, southward, and radial interplanetary magnetic fields (IMFs) are examined using three-dimensional global hybrid simulations. Energy conversion and entry of plasma and energy are weaker when the IMF is northward. After the IMF is southward, the inflow of the electromagnetic energy (the Poynting flux) increases, leading to a loading of magnetic energy. Subsequently, a strong energy conversion occurs from the magnetic field to the plasma, leading to an unloading of the magnetic energy. When the IMF is radial, strong disturbances are formed on the magnetopause, but the total ion flux, energy fluxes, and energy conversion are not pronounced. The corresponding ion enthalpy flux and bulk kinetic energy flux are also examined. These analyses allow precise and quantitative evaluations of various space weather effects.

Plain Language Summary The solar wind plasma, that is, ionized gas, moves fast toward Earth and interacts with the dipole magnetic field, forming the magnetosphere. Plasma and energy in the solar wind can enter the magnetosphere and are transported and converted therein, which can cause space weather. People have previously studied various ways in which plasma and energy can be transported and converted during the solar wind-magnetosphere interactions. However, the quantitative characteristics of these processes, for example, how many particles can enter the magnetosphere from the solar wind, and how fast is the entry process, have been studied much less because (a) spacecraft in situ observations cannot cover the entire domain of solar wind-magnetosphere interactions and (b) simulations need consider as much physics as possible given the limited computer resources. Using three-dimensional simulations that resolve both small-scale particle kinetics and global-scale dynamics, we study plasma transport and energy conversion during the interactions. More specifically, we calculate how much plasma and energy are transported and how much energy is converted from the magnetic field to the plasma in different ways and different stages of the interactions.

1. Introduction

Space weather is controlled by the solar wind-magnetosphere interaction, during which the energy and plasma in the solar wind can enter the magnetosphere through the magnetopause, the outer boundary of the magnetosphere (see review by Wing et al., 2014). The orientation of the magnetic field in the solar wind, referred to as the interplanetary magnetic field (IMF), dictates how the solar wind energy and plasma enter the magnetosphere and how they are converted and transported, respectively, therein (e.g., Dungey, 1961; Newell et al., 2007).

When the IMF is southward, it can allow efficient transport of plasma and energy through magnetic reconnection between the southward IMF and the northward geomagnetic field at the low-latitude magnetopause on the dayside (Ala-Lahti et al., 2022; Dai et al., 2024; Guo et al., 2021a, 2021b; Hasegawa et al., 2010; Lu, Fu, et al., 2022; Russell & Elphic, 1978; Tesema et al., 2024). The energy and plasma on the dayside can be convected toward the nightside magnetotail where magnetic reconnection can also occur to release the magnetic energy, and the energy and plasma are then transported both earthward and tailward after such magnetotail reconnection (Angelopoulos et al., 2008; Eastwood et al., 2010; Lu, Lu, et al., 2022; Lu, Wang, Lu, et al., 2020; Torbert et al., 2018). The earthward portion is injected into the inner magnetosphere, and the tailward portion is lost and returns to the solar wind (Angelopoulos et al., 1992, 1994; Kiehas et al., 2018; Lu, Lin et al., 2015; Lu, Lu et al., 2015; Slavin et al., 2003).

When the IMF is northward, energy and plasma can transport between the solar wind and the magnetosphere through the Kelvin–Helmholtz instability (KHI) at the low-latitude magnetopause on the flanks (Hasegawa et al., 2004; Johnson et al., 2014; Kavosi & Raeder, 2015). At the same time, the northward IMF can cause magnetic reconnection at the high-latitude magnetopause, which allows plasma entry into the high-latitude magnetosphere, and then the plasma can be injected into the cusps, illuminating auroral spots (Frey et al., 2003; Gosling et al., 1991; Guo et al., 2021c; Phan et al., 2003; Shi et al., 2013; Zhang et al., 2021).

More recent studies show that under radial IMF, ultra-low frequency (ULF) waves are formed in the foreshock and can propagate into the magnetosheath and even the magnetosphere (Lin & Wang, 2005; Sun et al., 2024). At the same time, high-speed jets are formed in the magnetosheath, which can strike the magnetopause to trigger surface waves and magnetic reconnection thereon, creating auroral signatures (Archer et al., 2019; Hietala et al., 2009, 2018; Wang et al., 2025). These processes may cause transfer of energy and plasma between the solar wind and the magnetosphere, which can even cause strong geomagnetic disturbances, such as substorms (Nykyri et al., 2019).

The above mechanisms of energy conversion and plasma transport during solar wind-magnetosphere interactions are mostly descriptive because they are obtained from limited spacecraft observations in vast space. To justify the importance of these mechanisms, it is crucial to examine them quantitatively. The previous quantitative analyses were based on either magnetohydrodynamic (MHD) simulations which lacked the crucial particle kinetics and the Hall effects (Brenner et al., 2021, 2023; Li et al., 2008; Lu et al., 2013, 2021; Palmroth et al., 2003, 2006) or hybrid simulations which were two-dimensional (2-D) and limited mostly to the dayside (Ala-Lahti et al., 2022). Here, using three-dimensional (3-D) global simulations with self-consistent particle tracing and particle kinetic effects, we quantify the energy conversion and plasma transport in the solar wind-magnetosphere system under different IMF conditions.

2. Simulation Model and Methods

A 3-D global hybrid simulation model (for details, see Lin et al., 2014; Lu, Guo, et al., 2022) is used here. Ions are treated as particles, and electrons are treated as a massless fluid. The simulation domain is $-60\,R_E \leq x \leq 20\,R_E$, $-32\,R_E \leq y \leq 32\,R_E$, $-32\,R_E \leq z \leq 32\,R_E$ in the geocentric solar magnetospheric (GSM) coordinate system, where R_E is Earth's radius. The boundary at $x = 20\,R_E$ is the fixed inflow boundary for the solar wind and IMF, and the outflow boundary conditions are utilized at the remaining five outer boundaries. An inner boundary is employed at $r = 3\,R_E$, which is linked to the ionosphere through magnetic field lines by incorporating ionospheric conditions with a uniform Pedersen conductance $\Sigma_P = 5$ S and a uniform Hall conductance $\Sigma_H = 10$ S. A loss-cone is applied at the inner boundary $r = 3\,R_E$. In our simulations, the loss cone angle is 13°, corresponding to an ionospheric loss cone angle of 2.5° (a widely accepted value).

Initially, the IMF and a 3-D dipole magnetic field are employed in the simulation domain. The initial dipole region is $x \leq 15\,R_E$, and the ions in this region has an initial density of 0.6 cm^{-3} and are referred to as the original magnetosphere ions, and the rest of the ions and the newly injected one from the solar wind are referred to as the solar wind ions. A current-dependent collision frequency is used to model the anomalous resistivity, with a typical peak collision frequency of $\sim 0.1\,\Omega_i$, where Ω_i is the ion gyrofrequency in the solar wind. The electrons are assumed to be isothermal. The time step is $\Delta t = 0.02\,\Omega_i^{-1}$. About 5×10^9 particles are used in the simulation. The velocity, density and ion temperature of the solar wind are 700 km/s in the $-x$ direction, 6 cm^{-3}, and 10 eV, respectively. The solar wind ion inertial length is chosen to be 0.1 R_E. Nonuniform gridding is employed, with a grid size of 0.2 R_E in the near-Earth region (Figure S1 in Supporting Information S1). Such a resolution is small enough to resolve the dominant ion kinetic modes in the solar wind and the magnetosheath as well as the complete ion kinetics in the magnetotail (where the density is low and the local ion inertial length is larger than in the solar wind).

Two cases are simulated. In both cases, the IMF starts northward with $B_0 = 10$ nT. The IMF changes from northward to southward and radial by adopting a tangential discontinuity (TD) and a rotational discontinuity (RD) in Cases 1 and 2, respectively. The discontinuities are at $x = 450\,R_E$ when $t = 0$, and they propagate earthward along with the solar wind.

We identify the magnetopause using the parameter $\beta^* = (P_{th} + P_{dyn})/P_{mag}$, where P_{th} is the plasma thermal pressure, P_{dyn} is the dynamic pressure, and P_{mag} is the magnetic pressure. To define the magnetopause, β^* ranges
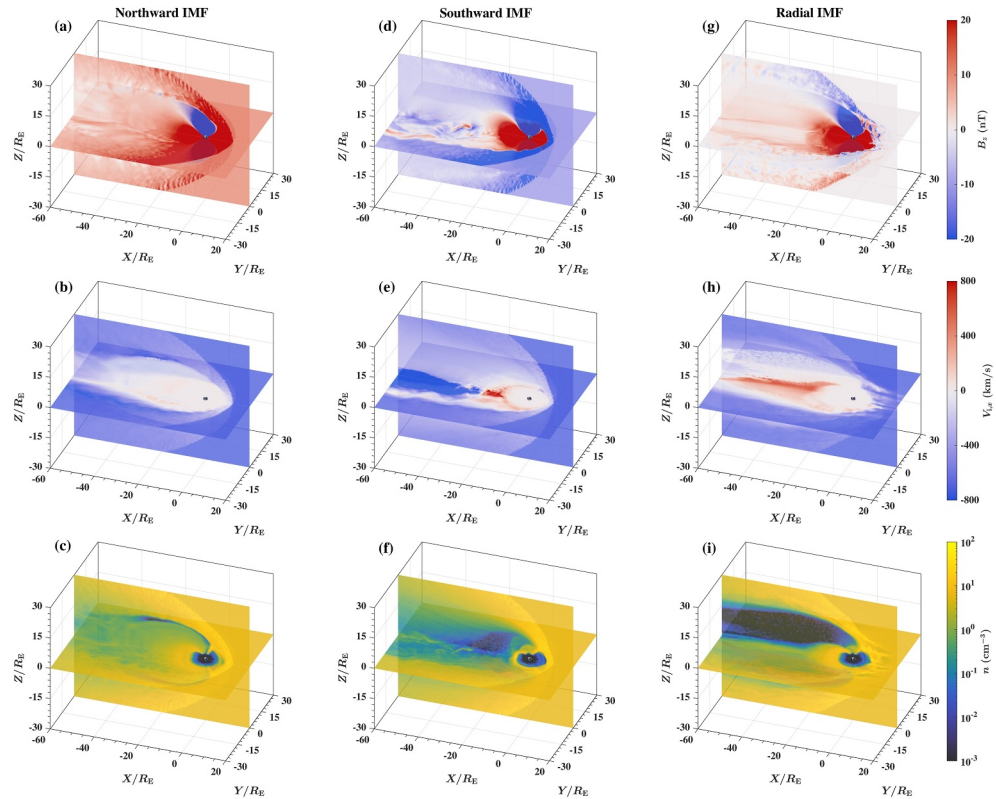
Figure 1. (a, d, g) Magnetic field B_z, (b, e, h) ion velocity V_{ix}, and (c, f, i) plasma density n in the equatorial plane and the meridian plane when the IMF is northward at the representative time $t = 3{,}779$ s in Case 1 (same for Case 2 because the northward period is similar in the two cases), southward at the representative time $t = 6{,}859$ s in Case 1, and radial at the representative time $t = 6{,}859$ s in Case 2, respectively.

typically from 0.1 to 1.5 (Ala-Lahti et al., 2022; Brenner et al., 2021; Xu et al., 2016), and here we use $\beta^* = 0.2$. To include the magnetotail in the magnetosphere, we let P_{dyn} less than 1 nPa. A 3-D smoothing method of "box," that is, weighted moving average over each window of volume, is applied to the identified magnetopause. The box size is $5 \times 5 \times 5$ grids.

3. Simulation Results

The interaction between the solar wind and the magnetosphere forms the bow shock, magnetopause, and magnetotail self-consistently in our simulations. When the IMF is northward, the magnetotail is quiet without occurrence of magnetic reconnection, so there is no negative B_z or fast flow in the magnetotail (Figures 1a and 1b). Because of the absence of magnetic reconnection, the plasma is well-preserved in the magnetotail with a density ≈ 2 cm^{-3} (Figure 1c).

When the IMF is southward (Case 1), reversals of B_z and bi-directional plasma flows with a velocity ≈ 800 km/s in the x direction (Figures 1d and 1e) indicate the occurrence of magnetotail reconnection at $x \approx -20\ R_E$. Such strong reconnection evacuates the plasma at the reconnection site (also see, e.g., Lu, Wang, Wang, et al., 2020); therefore, the density near the reconnection site decreases to 0.02 cm^{-3} at $x \approx -20\ R_E$ (Figure 1f). Reconnection also forms a large-scale plasmoid which has a high density and moves tailward. At the representative time shown in Figures 1d–1f, the plasmoid moves to $x \approx -50\ R_E$, and the density ≈ 5 cm^{-3} therein (Figure 1f). The earthward flow transports the plasma and magnetic flux toward the Earth, increasing the plasma density and magnetic field B_z cumulatively in the near-Earth tail within $\sim 10\ R_E$ (Figures 1d and 1f) where the earthward fast flow decelerates (Figure 1e).

When the IMF is radial (Case 2), the bow shock and the magnetosheath become more fluctuated and are permeated by waves and high-speed jets. The waves have a period of 31.3 s and thus a frequency of 0.032 Hz
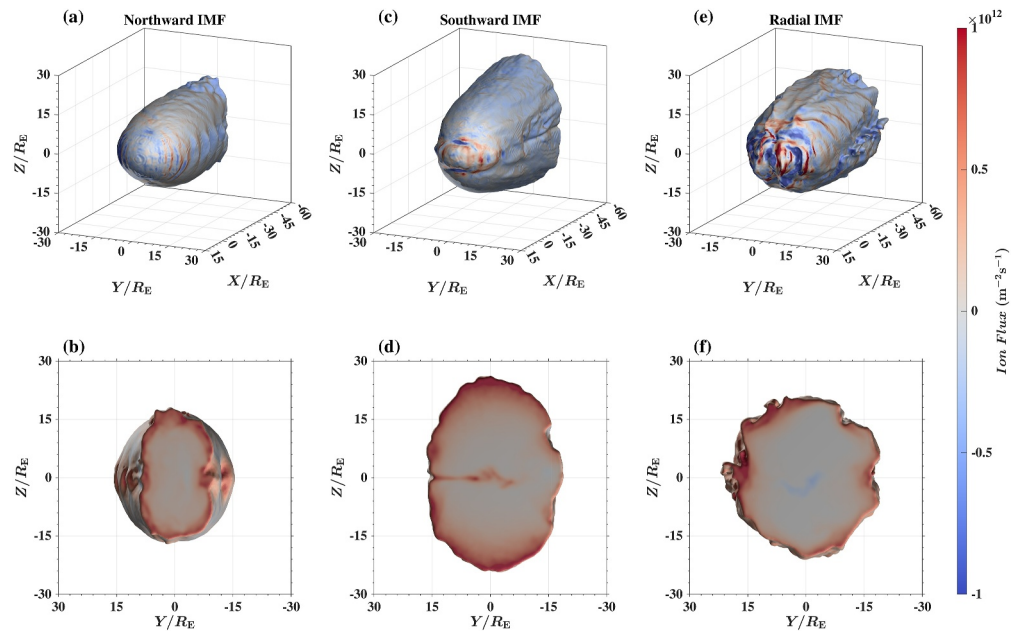
Figure 2. The normal component of the ion flux $n\mathbf{V}_i$ on the magnetopause and the magnetotail plane at $x = -50\, R_E$ when the IMF is (a, b) northward at the representative time $t = 3{,}779$ s in Case 1 (same for Case 2 because the northward period is similar in the two cases), (c, d) southward at the representative time $t = 6{,}859$ s in Case 1, and (e, f) radial at the representative time $t = 6{,}859$ s in Case 2, respectively. The magnetopause and the magnetotail plane constitute a closed surface A which encloses the volume V of the magnetosphere. The upper panels are from a flank viewpoint and the bottom panels are from a tail viewpoint.

(Figure S2 in Supporting Information S1 and the analysis in the figure caption), showing that they are typical ULF waves with wavy perpendicular magnetic components B_z (Figure 1g) and B_y (Figure S2 in Supporting Information S1), which are formed at the foreshock and amplified in the magnetosheath (Wang et al., 2024). The high-speed jets are characterized by increases in flow velocity up to 600 km/s (Figure 1h and Figure S3 in Supporting Information S1) and plasma density up to 50 cm^{-3} (Figure 1i and Figure S3 in Supporting Information S1). The scale size parallel and perpendicular to the propagation direction of the jets is about 5 R_E and 1 R_E, respectively (Figure S3 in Supporting Information S1). On the nightside, a thin current sheet is formed, with a plasma density ≈ 2 cm^{-3}. The absence of bidirectional flow indicates that magnetic reconnection does not occur in the current sheet (not until the end of the simulation). Instead, a strong earthward flow at a velocity of ~ 800 km/s is caused by a large Lorentz force in the thin current sheet (Figure 1h). The plasma density is low in the lobe region (see Figure 1i), much lower than under northward and southward IMFs.

Figure 2a shows the shape of the magnetopause and the ion flux $n\mathbf{V}_i$ normal to the magnetopause under northward IMF. The wavy structure resembles the dynamics of the KHI. The wavelength of the KHI on the magnetopause ranges from 4 R_E near Earth to 12 R_E at distant tail. The nightside magnetosphere is eroded, and the dayside magnetosphere is replenished, which can be attributed to the high-latitude magnetic reconnection between the IMF and the lobe magnetic field. The standoff distance of the dayside magnetopause is 9.1 R_E, and the nightside magnetopause extends to $z \approx \pm 15\, R_E$ at $x = -50\, R_E$.

When the IMF is southward, the magnetosphere is eroded on the dayside and replenished on the nightside, which can be attributed to magnetic reconnection at low-latitude dayside magnetopause. The standoff distance of the dayside magnetopause is decreased to 7.9 R_E, and the nightside magnetopause is expanded to $z \approx \pm 25\, R_E$ at $x = -50\, R_E$. The negative ion flux normal to the nightside magnetopause indicates that the plasma flows into the magnetosphere on the nightside (Figure 2c).

When the IMF is radial, the magnetopause is highly disturbed, especially on the dayside, with the ion flux (flowing both into and out of the magnetosphere) much larger than under northward and southward IMFs (Figure 2e). From the tail viewpoint (Figures 2b, 2d, and 2f), the plasma flows tailward from the central current sheet only when the IMF is southward (Figure 2d), and this is because of the tailward reconnection outflow. After
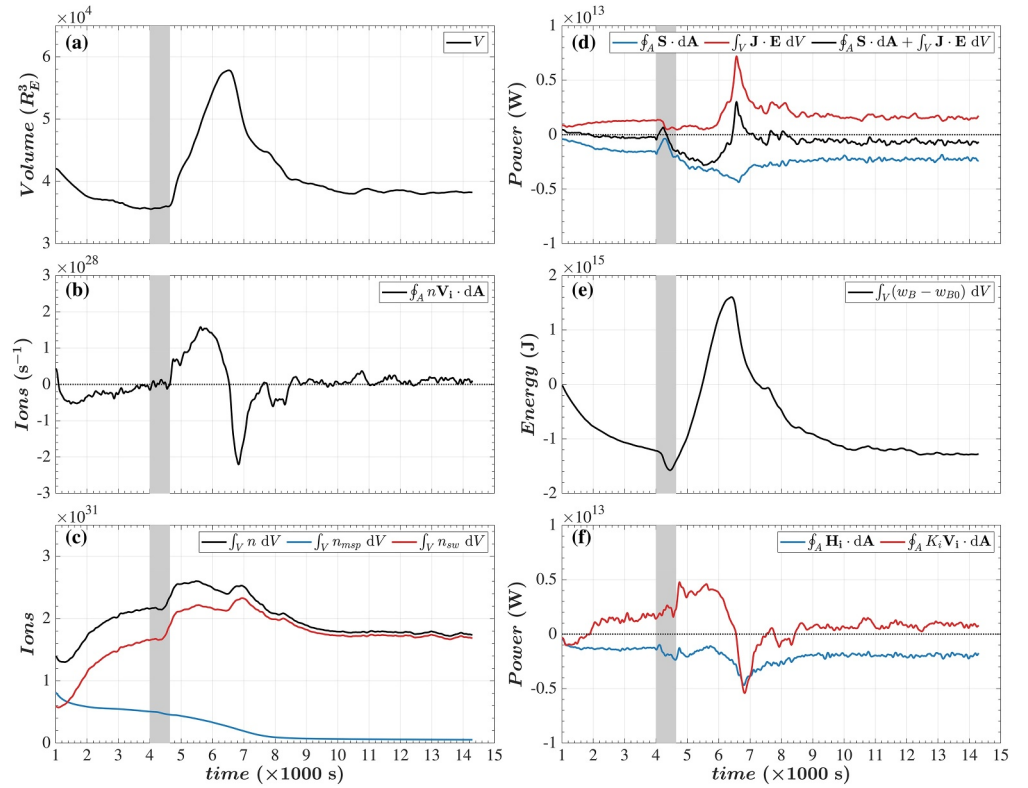
Figure 3. For Case 1 in which the IMF changes from northward to southward. (a) Volume of the magnetosphere enclosed by the surface A, (b) total ion flux integrated over A, $\oint_A n\mathbf{V}_i \cdot d\mathbf{A}$, (c) number of ions integrated in V, $\int_V n \, dV$ (black), and the numbers of the original magnetosphere ions $\int_V n_{msp} \, dV$ (blue) and the ions originated from the solar wind $\int_V n_{sw} \, dV$ (red), (d) total Poynting flux integrated over A, $\oint_A \mathbf{S} \cdot d\mathbf{A}$ (red), energy conversion rate integrated in V, $\int_V \mathbf{j} \cdot \mathbf{E} \, dV$ (blue), and sum of the two terms (black), (e) change in magnetic energy from $t = 1,000$ s, and (f) total ion enthalpy flux integrated over A, $\oint_A \mathbf{H}_i \cdot d\mathbf{A}$ (red), and total ion bulk kinetic energy flux integrated over A, $\oint_A K_i \mathbf{V}_i \cdot d\mathbf{A}$ (blue), where $K_i = nm_i V_i^2/2$ is the bulk kinetic energy density, $\mathbf{H}_i = U_i \mathbf{V}_i + \overset{\leftrightarrow}{\mathbf{P}}_i \cdot \mathbf{V}_i$ is the enthalpy flux, $U_i = (P_{i\parallel} + 2P_{i\perp})/3$ is the thermal energy density, $\mathbf{V}_i$ is the ion flow velocity, and $\overset{\leftrightarrow}{\mathbf{P}}_i$ is the ion pressure tensor. The gray shaded region represents the period when the TD (that flanks the northward and southward IMFs) interacts with the magnetopause.

the IMF changes from northward to radial, the nightside magnetopause expands and has a more circular cross-section (Figure 2f). Note that the KHI is less pronounced under southward and radial IMFs than under northward IMF (see Figure 2 and Figure S4 in Supporting Information S1). More details of the two cases are given in Supporting Information S1.

In Figures 3 and 4, we analyze the plasma transport and energy conversion for Cases 1 and 2, respectively. The magnetopause and the tailward boundary constitute a closed surface A which encloses the volume V of the magnetosphere. The plasma transport is governed by

$$\frac{\partial n}{\partial t} = -\nabla \cdot (n\mathbf{V}_i). \tag{1}$$

Based on the Reynolds transport theorem, that is, by integrating Equation 1 over V and considering the motion of the magnetopause, we have

$$\frac{d}{dt}\left(\int_V n \, dV\right) = -\oint_A n\mathbf{V}_i \cdot d\mathbf{A} + \oint_A n\mathbf{V}_{MP} \cdot d\mathbf{A}, \tag{2}$$
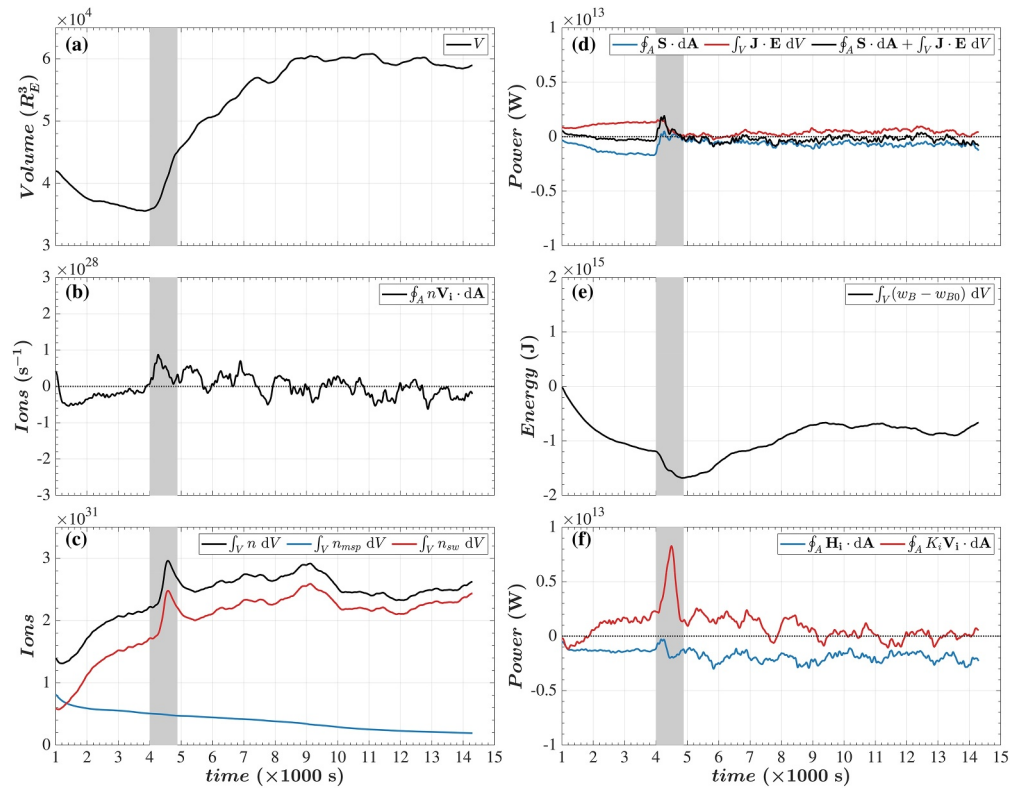
Figure 4. Same format as Figure 3, but for Case 2 in which the IMF changes from northward to radial. The gray shaded region represents the period when the RD (that flanks the northward and radial IMFs) interacts with the magnetopause.

where $\mathbf{V}_{MP}$ is the velocity of the magnetopause, and the second term on the right-hand-side is the amendment caused by the motion of the magnetopause. For example, the expansion of the magnetopause, that is, the increase in the volume V of the magnetosphere, leads to an increase in the total ion number.

During the northward IMF, until $t \approx 4,000$ s, the negative total ion flux on the order of 10^{27} s^{-1} (Figure 3b) indicates that the plasma is transported into the magnetosphere, and the total ion number $\int_V n \, dV$ increases (Figure 3c). The possible plasma entry channels could be the high-latitude magnetopause reconnection and the KHI. Although the dayside magnetosphere is inflated, the high-latitude magnetopause reconnection erodes the nightside magnetosphere, and the magnetotail is much larger than the dayside magnetosphere, therefore, the volume V of the magnetosphere decreases (Figure 3a).

In Case 1, the IMF is southward after $t \approx 4,600$ s, and strong magnetotail reconnection emerges, which causes loss of plasma through the tailward outflow and plasmoids. Therefore, the total ion flux becomes positive until $t \approx 6,500$ s, with a much higher efficiency of transport, 1.5×10^{28} s^{-1} (Figure 3b). The total ion flux is the net outcome of the competition between the gain from the magnetopause and the loss from the magnetotail. During this period, from $t \approx 4,600 - 6,500$ s, the magnetosphere volume V increases rapidly to nearly 6×10^4 R_E^3 (Figure 3a), which is because the nightside magnetosphere is replenished by the magnetic flux originated from the dayside magnetopause reconnection. The competing impacts of the plasma loss from the magnetotail (first right-hand-side term in Equation 2) and the magnetopause expansion (second right-hand-side term in Equation 2) leads to an increase followed by a decrease in the total ion number in the magnetosphere during this period (Figure 3c).

After $t \approx 6,500$ s, the magnetosphere volume V decreases first rapidly and then slowly to about 3.8×10^4 R_E^3 (Figure 3a). At the same time, many particles enter the magnetosphere through the magnetopause as indicated by the negative peak in the net ion flux (Figure 3b), which corresponds to an increase in the total ion number at $t \approx 7000$ s. Soon after $t \approx 7,000$ s, the total ion number begins to decrease again (Figure 3c), and according to Equation 2, this is mainly attributed to the decrease in V, that is, the deflation of the magnetosphere. Such decrease stops at $t \approx 10,000$ s when the system becomes quasistatic.

We divide the ions into two populations, the original magnetosphere ions and the solar wind ions. (In our simulations, the ions in the inner magnetosphere at $r < 7.5\ R_E$ are considered as a cold fluid, so these ions are excluded from the analysis here.) Figure 3c shows that the solar wind ions (red) can easily enter the magnetosphere and soon becomes dominant. The original magnetosphere ions (blue) can be retained well under northward IMF but are soon lost under southward IMF (especially after the strong magnetotail reconnection at $t \approx 6{,}500$ s). The original magnetosphere plasma is almost all replaced by the solar wind plasma within ~2 hr.

The conversion between the magnetic energy and ion energy is governed by

$$\partial w_B / \partial t = -\nabla \cdot \mathbf{S} - \mathbf{j} \cdot \mathbf{E}, \tag{3}$$

and like Equation 2, we have

$$\frac{\mathrm{d}}{\mathrm{d}t}\left(\int_V w_B\,\mathrm{d}V\right) = -\oint_A \mathbf{S} \cdot \mathrm{d}\mathbf{A} - \int_V \mathbf{j} \cdot \mathbf{E}\,\mathrm{d}V + \oint_A w_B \mathbf{V}_{MP} \cdot \mathrm{d}\mathbf{A}, \tag{4}$$

where $w_B = B^2/(2\mu_0)$ is the magnetic energy density, and $\mathbf{S}$ is the Poynting flux. In Case 1, the total Poynting flux $\oint_A \mathbf{S} \cdot \mathrm{d}\mathbf{A}$ is always negative, indicating that there is always a net inflow of the electromagnetic energy into the magnetosphere. During the northward IMF until $t \approx 4000$ s, $\left|\oint_A \mathbf{S} \cdot \mathrm{d}\mathbf{A}\right|$ is within 2×10^{12} W. On the other hand, the power of energy conversion from the magnetic field to the plasma, $\int_V \mathbf{j} \cdot \mathbf{E}\,\mathrm{d}V$, is even smaller, about 1×10^{12} W, which should give a small increase in the total magnetic energy. However, according to the third right-hand-side term in Equation 4, the shrinkage of the magnetopause, that is, the decrease in the volume of the magnetosphere (Figure 3a) causes the decrease in the total magnetic energy $\int_V w_B\,\mathrm{d}V$ (Figure 3e).

During the southward IMF (after $t \approx 4600$ s) both the electromagnetic energy gain from the Poynting flux $\left|\oint_A \mathbf{S} \cdot \mathrm{d}\mathbf{A}\right|$ and the loss to the plasma $\int_V \mathbf{j} \cdot \mathbf{E}\,\mathrm{d}V$ increase. These two effects compete, which first causes a loading of the magnetic energy by the net inflow of the Poynting flux, and then after the strong magnetotail reconnection occurs at $t \approx 6{,}500$ s, the large $\int_V \mathbf{j} \cdot \mathbf{E}\,\mathrm{d}V$ up to $\sim 7 \times 10^{12}$ W causes an unloading of the magnetic energy by (Figure 3d). After $t \approx 8{,}000$ s, $\left|\oint_A \mathbf{S} \cdot \mathrm{d}\mathbf{A}\right|$ and $\int_V \mathbf{j} \cdot \mathbf{E}\,\mathrm{d}V$ are both $\sim 2 \times 10^{12}$ W, showing that the magnetosphere is in a quasistatic state, that is, the net inflow of the electromagnetic energy is all converted to the plasma energy. Overall, after the southward turning of the IMF, a loading and then an unloading of magnetic energy $\approx 3 \times 10^{15}$ J occur in ~1 hr (Figure 3e). In addition to the Poynting flux, there are also enthalpy flux and bulk kinetic energy flux across the magnetopause, as shown in Figure 3f. Like the Poynting flux, the ion enthalpy flux is always negative, indicating a net inflow of the thermal energy; on the other hand, the ion bulk kinetic energy flux is first outward until $t \approx 6500$ s, which is followed by a rapid inward compensation and a slow recovery.

In Case 2, the northward IMF period until $t \approx 4000$ s is the same as in Case 1. At $t \approx 4{,}000 - 4{,}900$ s, when the RD (that flanks the northward to radial IMFs) interacts with the bow shock and the magnetopause, the magnetosphere expands abruptly (Figure 4a), coexisting with an impulsive net outflow of the ions and the ion bulk kinetic energy flux (Figures 4b and 4f). According to the second right-hand-side term in Equation 2, such a sudden expansion of the magnetosphere leads to an impulsive increase in the number of ions (mostly solar wind ions) in the magnetosphere (Figure 4c).

After $t \approx 4{,}900$ s, the IMF becomes radial, and the total ion flux, the total Poynting flux, and the total power of energy conversion (Figures 4b and 4d) are all small, indicating that the radial IMF leads to little plasma transport and energy conversion. The volume of the magnetosphere keeps increasing (Figure 4a) because radial IMF no longer has the magnetic tension to pinch the magnetopause (the field lines are shown in Figure 1 in Lin & Wang, 2005). Although the first two right-hand-side terms in Equation 4 are small under radial IMF, the magnetic energy increases (Figure 4e) because of the increase in the volume of the magnetosphere (i.e., the third right-hand-side term in Equation 4 is dominant). However, the absence of magnetotail reconnection renders the increase in energy less efficient than under southward IMF. Because of this, the loss of the original magnetosphere ions (blue curve in Figure 4c) is much slower than under southward IMF. The ion enthalpy flux in Case 2 is also negative, indicating a net inflow of the thermal energy (Figure 4f).

4. Summary and Discussion

Plasma transport and energy conversion during solar wind-magnetosphere interactions under northward, southward, and radial IMFs are examined using 3-D global hybrid simulations. The main findings are summarized below.

1. When the IMF is northward, the magnetosphere expands on the dayside and shrinks on the nightside. The number of particles in the magnetosphere increases; the volume of the magnetosphere and the magnetic energy therein decrease. Particles and electromagnetic energy flow into the magnetosphere slowly at low rates. Magnetic reconnection does not occur in the magnetotail plasma sheet so that the particles in the magnetosphere are well preserved.

2. When the IMF is southward, the magnetosphere shrinks on the dayside and expands on the nightside, corresponding to a strong inflow in Poynting flux and a strong particle outflow. Strong magnetic reconnection occurs, and a strong energy conversion from the magnetic field to the plasma. Such processes under southward IMF cause a loading and then an unloading of magnetic energy $\approx 3 \times 10^{15}$ J in ~1 hr. At the same time, the volume of the magnetosphere increases by a factor of ~1.6 during loading and then recovers during unloading. After the strong magnetotail reconnection, the original magnetosphere particles are mostly lost, which are replaced by the particles from the solar wind, corresponding to a strong particle inflow into the magnetosphere.

3. When the IMF is radial, strong disturbances are generated on the magnetopause, and the volume of the magnetosphere increases. Despite of the strong disturbances, the total ion flux across the magnetopause is small. At the same time, the total Poynting flux across the magnetopause and the total energy conversion in the magnetosphere are also small, even smaller than those under northward IMF.

Our simulations show that the shape of the magnetopause varies significantly under different IMF conditions (see Figure 2). When the IMF is northward, the magnetopause expands on the dayside and shrinks on the nightside; when the IMF is southward, the magnetopause shrinks on the dayside and expands on the nightside. These are consistent with previous MHD simulation (e.g., Lu et al., 2011). The magnetopause is more active under radial IMF with prominent disturbances (Figures 2e and 2f). The disturbances are believed to be caused by waves and high-speed jets in the magnetosheath, which cannot be resolved by MHD simulations. Although there are some hybrid simulations of the waves and jets, they are either 2-D (Guo et al., 2022; Suni et al., 2021; Turc et al., 2023) or limited to the dayside (Chen et al., 2021; Fatemi et al., 2024; Ren et al., 2024). Moreover, the discontinuities can interact with the shock and the magnetopause, introducing various phenomena. For example, TDs can be compressed in the magnetosheath to allow occurrence of magnetic reconnection therein (e.g., Pang et al., 2010), and RDs can also form foreshock transients (e.g., hot flow anomalies and foreshock bubbles, e.g., Lin, 1997, 2002) that are responsible for the impulsive increases in the shaded region in Figure 4.

We show that when the IMF is northward, the ion flux and Poynting flux are smaller than those under southward IMF (Figures 3b and 3d), which is consistent with previous MHD simulations (Lu et al., 2013). The strong magnetotail reconnection and large tailward moving plasmoid suggest the occurrence of a substorm under southward IMF (see Baker et al., 1996; and references therein). Moreover, such processes cause loading and then unloading of magnetic energy of ~3×10^{15} J within ~1 hr (Figure 3e). This is consistent with the typical energy budget and time scale of substorms (e.g., Spencer et al., 2019; Stern, 1984). The energy loading and unloading has also been well described by MHD simulations (e.g., Brenner et al., 2023, and references therein). When the IMF is radial, we show that although the magnetopause disturbances are strong, the total plasma transport and energy conversion are weak, even weaker than under northward IMF. In contrast, previous MHD simulations show that the energy transfer under radial IMF is stronger than under northward IMF (Lu et al., 2021). This discrepancy may be attributed to the magnetopause disturbances, which needs further investigations.

The following effects have not been considered in our study yet. (a) Our hybrid simulations use prescribed, steady solar wind and IMF, which is less practical than the real-time solar wind and IMF used in many previous MHD simulations (e.g., Jing et al., 2014; Palmroth et al., 2003; Zhang et al., 2024), (b) Although our simulations include an ionospheric module, we adopt a simple ionospheric conductance (uniform and time-independent). Realistic ionospheric conductance has been shown to play an important role in controlling the magnetospheric dynamics (e.g., Lotko et al., 2014), and the loss cone angle at the ionosphere may also affect our results. (c) To save computer resource, like other hybrid simulations, our simulations are scaled down for several times by adopting a larger-than-realistic solar wind ion inertial length of $0.1\ R_E$. Although it has been shown that this does not affect

the structure and dynamics/kinetics of the system (Lin et al., 2014; Omidi et al., 2004), some mesoscale physics may be affected, which needs to be examined using a more realistic ratio between the kinetic and macroscopic scales. (d) Quantification of plasma transport and energy conversion depends highly on how one identifies the magnetopause (Yi et al., 2025). More sophisticatedly, one needs to examine the energy transfer/conversion in and between different subregions of the magnetosphere (e.g., Brenner et al., 2023; Lu et al., 2013). The above effects are important and left for future studies.

Data Availability Statement

The simulation data produced in this study can be obtained from Guo and Lu (2024).

References

Ala-Lahti, M., Pulkkinen, T. I., Pfau-Kempf, Y., Grandin, M., & Palmroth, M. (2022). Energy flux through the magnetopause during flux transfer events in hybrid-vlasov 2D simulations. *Geophysical Research Letters*, *49*(19), e2022GL100079. https://doi.org/10.1029/2022GL100079

Angelopoulos, V., Baumjohann, W., Kennel, C. F., Coroniti, F. V., Kivelson, M. G., Pellat, R., et al. (1992). Bursty bulk flows in the inner central plasma sheet. *Journal of Geophysical Research: Space*, *97*(A4), 4027–4039. https://doi.org/10.1029/91ja02701

Angelopoulos, V., Kennel, C. F., Coroniti, F. V., Pellat, R., Kivelson, M. G., Walker, R. J., et al. (1994). Statistical characteristics of bursty bulk flow events. *Journal of Geophysical Research: Space*, *99*(A11), 21257–21280. https://doi.org/10.1029/94ja01263

Angelopoulos, V., McFadden, J. P., Larson, D., Carlson, C. W., Mende, S. B., Frey, H., et al. (2008). Tail reconnection triggering substorm onset. *Science*, *321*(5891), 931–935. https://doi.org/10.1126/science.1160495

Archer, M. O., Hietala, H., Hartinger, M. D., Plaschke, F., & Angelopoulos, V. (2019). Direct observations of a surface eigenmode of the dayside magnetopause. *Nature Communications*, *10*(1), 615. https://doi.org/10.1038/s41467-018-08134-5

Baker, D. N., Pulkkinen, T. I., Angelopoulos, V., Baumjohann, W., & McPherron, R. L. (1996). Neutral line model of substorms: Past results and present view. *Journal of Geophysical Research: Space*, *101*(A6), 12975–13010. https://doi.org/10.1029/95ja03753

Brenner, A., Pulkkinen, T. I., Al Shidi, Q., & Toth, G. (2021). Stormtime energetics: Energy transport across the magnetopause in a global MHD simulation. *Frontiers in Astronomy and Space Sciences*, *8*, 756732. https://doi.org/10.3389/fspas.2021.756732

Brenner, A., Pulkkinen, T. I., Al Shidi, Q., & Toth, G. (2023). Dissecting Earth's magnetosphere: 3D energy transport in a simulation of a real storm event. *Journal of Geophysical Research: Space*, *128*(11), e2023JA031899. https://doi.org/10.1029/2023JA031899

Chen, L. J., Ng, J., Omelchenko, Y., & Wang, S. (2021). Magnetopause reconnection and indents induced by foreshock turbulence. *Geophysical Research Letters*, *48*(11), e2021GL093029. https://doi.org/10.1029/2021GL093029

Dai, L., Zhu, M. H., Ren, Y., Gonzalez, W., Wang, C., Sibeck, D., et al. (2024). Global-scale magnetosphere convection driven by dayside magnetic reconnection. *Nature Communications*, *15*(1), 639. https://doi.org/10.1038/s41467-024-44992-y

Dungey, J. W. (1961). Interplanetary magnetic field and auroral zones. *Physical Review Letters*, *6*(2), 47–48. https://doi.org/10.1103/PhysRevLett.6.47

Eastwood, J. P., Phan, T. D., Oieroset, M., & Shay, M. A. (2010). Average properties of the magnetic reconnection ion diffusion region in the Earth's magnetotail: The 2001-2005 Cluster observations and comparison with simulations. *Journal of Geophysical Research: Space*, *115*(A8), A08215. https://doi.org/10.1029/2009ja014962

Fatemi, S., Hamrin, M., Krämer, E., Gunell, H., Nordin, G., Karlsson, T., & Goncharov, O. (2024). Unveiling the 3D structure of magnetosheath jets. *Monthly Notices of the Royal Astronomical Society*, *531*(4), 4692–4713. https://doi.org/10.1093/mnras/stae1456

Frey, H. U., Phan, T. D., Fuselier, S. A., & Mende, S. B. (2003). Continuous magnetic reconnection at Earth's magnetopause. *Nature*, *426*(6966), 533–537. https://doi.org/10.1038/nature02084

Gosling, J. T., Thomsen, M. F., Bame, S. J., Elphic, R. C., & Russell, C. T. (1991). Observations of reconnection of interplanetary and lobe magnetic-field lines at the high-latitude magnetopause. *Journal of Geophysical Research: Space*, *96*(A8), 14097–14106. https://doi.org/10.1029/91ja01139

Guo, J., & Lu, S. (2024). Data for mass transport and energy conversion at Earth [Dataset]. *Science Data Bank*. https://doi.org/10.57760/sciencedb.space.02165

Guo, J., Lu, S., Lu, Q. M., Lin, Y., Wang, X. Y., Huang, K., et al. (2021a). Re-reconnection processes of magnetopause flux ropes: Three-dimensional global hybrid simulations. *Journal of Geophysical Research: Space*, *126*(6), e2021JA029388. https://doi.org/10.1029/2021JA029388

Guo, J., Lu, S., Lu, Q. M., Lin, Y., Wang, X. Y., Huang, K., et al. (2021b). Structure and coalescence of magnetopause flux ropes and their dependence on IMF clock angle: Three-dimensional global hybrid simulations. *Journal of Geophysical Research: Space*, *126*(2), e2020JA028670. https://doi.org/10.1029/2020JA028670

Guo, J., Lu, S., Lu, Q. M., Lin, Y., Wang, X. Y., Ren, J. Y., et al. (2022). Large-scale high-speed jets in Earth's magnetosheath: Global hybrid simulations. *Journal of Geophysical Research: Space*, *127*(6), e2022JA030477. https://doi.org/10.1029/2022JA030477

Guo, J., Lu, S., Lu, Q. M., Lin, Y., Wang, X. Y., Zhang, Q. H., et al. (2021c). Three-dimensional global hybrid simulations of high latitude magnetopause reconnection and flux ropes during the northward IMF. *Geophysical Research Letters*, *48*(21), e2021GL095003. https://doi.org/10.1029/2021GL095003

Hasegawa, H., Fujimoto, M., Phan, T. D., Rème, H., Balogh, A., Dunlop, M. W., et al. (2004). Transport of solar wind into Earth's magnetosphere through rolled-up Kelvin-Helmholtz vortices. *Nature*, *430*(7001), 755–758. https://doi.org/10.1038/nature02799

Hasegawa, H., Wang, J., Dunlop, M. W., Pu, Z. Y., Zhang, Q. H., Lavraud, B., et al. (2010). Evidence for a flux transfer event generated by multiple X-line reconnection at the magnetopause. *Geophysical Research Letters*, *37*(16), L16101. https://doi.org/10.1029/2010gl044219

Hietala, H., Laitinen, T. V., Andréeová, K., Vainio, R., Vaivads, A., Palmroth, M., et al. (2009). Supermagnetosonic jets behind a collisionless quasiparallel shock. *Physical Review Letters*, *103*(24), 245001. https://doi.org/10.1103/physrevlett.103.245001

Hietala, H., Phan, T. D., Angelopoulos, V., Oieroset, M., Archer, M. O., Karlsson, T., & Plaschke, F. (2018). In situ observations of a magnetosheath high-speed jet triggering magnetopause reconnection. *Geophysical Research Letters*, *45*(4), 1732–1740. https://doi.org/10.1002/2017gl076525

Jing, H., Lu, J. Y., Kabin, K., Zhao, J. S., Liu, Z. Q., Yang, Y. F., et al. (2014). MHD simulation of energy transfer across magnetopause during sudden changes of the IMF orientation. *Planetary and Space Science*, *97*, 50–59. https://doi.org/10.1016/j.pss.2014.04.001

Johnson, J. R., Wing, S., & Delamere, P. A. (2014). Kelvin Helmholtz instability in planetary magnetospheres. *Space Science Reviews*, *184*(1–4), 1–31. https://doi.org/10.1007/s11214-014-0085-z

Kavosi, S., & Raeder, J. (2015). Ubiquity of Kelvin-Helmholtz waves at Earth's magnetopause. *Nature Communications*, *6*(1), 7019. https://doi.org/10.1038/ncomms8019

Kiehas, S. A., Runov, A., Angelopolos, V., Hietala, H., & Korovinksiy, D. (2018). Magnetotail fast flow occurrence rate and dawn-dusk asymmetry at X_{GSM} ~-60 R_E. *Journal of Geophysical Research: Space*, *123*(3), 1767–1778. https://doi.org/10.1002/2017ja024776

Li, W. H., Raeder, J., Thomsen, M. F., & Lavraud, B. (2008). Solar wind plasma entry into the magnetosphere under northward IMF conditions. *Journal of Geophysical Research: Space*, *113*(A4), A04204. https://doi.org/10.1029/2007ja012604

Lin, Y. (1997). Generation of anomalous flows near the bow shock by its interaction with interplanetary discontinuities. *Journal of Geophysical Research: Space*, *102*(A11), 24265–24281. https://doi.org/10.1029/97ja01989

Lin, Y. (2002). Global hybrid simulation of hot flow anomalies near the bow shock and in the magnetosheath. *Planetary and Space Science*, *50*(5–6), 577–591. https://doi.org/10.1016/S0032-0633(02)00037-5

Lin, Y., & Wang, X. Y. (2005). Three-dimensional global hybrid simulation of dayside dynamics associated with the quasi-parallel bow shock. *Journal of Geophysical Research: Space*, *110*(A12), A12216. https://doi.org/10.1029/2005ja011243

Lin, Y., Wang, X. Y., Lu, S., Perez, J. D., & Lu, Q. (2014). Investigation of storm time magnetotail and ion injection using three-dimensional global hybrid simulation. *Journal of Geophysical Research: Space*, *119*(9), 7413–7432. https://doi.org/10.1002/2014ja020005

Lotko, W., Smith, R. H., Zhang, B. Z., Ouellette, J. E., Brambles, O. J., & Lyon, J. G. (2014). Ionospheric control of magnetotail reconnection. *Science*, *345*(6193), 184–187. https://doi.org/10.1126/science.1252907

Lu, J. Y., Jing, H., Liu, Z. Q., Kabin, K., & Jiang, Y. (2013). Energy transfer across the magnetopause for northward and southward interplanetary magnetic fields. *Journal of Geophysical Research: Space*, *118*(5), 2021–2033. https://doi.org/10.1002/jgra.50093

Lu, J. Y., Liu, Z. Q., Kabin, K., Zhao, M. X., Liu, D. D., Zhou, Q., & Xiao, Y. (2011). Three dimensional shape of the magnetopause: Global MHD results. *Journal of Geophysical Research: Space*, *116*(A9), A09237. https://doi.org/10.1029/2010ja016418

Lu, J. Y., Zhang, H. X., Wang, M., Kabin, K., Zhou, Y., & Li, J. Y. (2021). Energy transfer across the magnetopause under radial IMF conditions. *The Astrophysical Journal*, *920*(1), 52. https://doi.org/10.3847/1538-4357/ac15f4

Lu, Q. M., Fu, H. S., Wang, R. S., & Lu, S. (2022). Collisionless magnetic reconnection in the magnetosphere. *Chinese Physics B*, *31*(8), 089401. https://doi.org/10.1088/1674-1056/ac76ab

Lu, Q. M., Guo, J., Lu, S., Wang, X. Y., Slavin, J. A., Sun, W. J., et al. (2022). Three-dimensional global hybrid simulations of flux transfer event showers at Mercury. *The Astrophysical Journal*, *937*(1), 1. https://doi.org/10.3847/1538-4357/ac8bcf

Lu, Q. M., Wang, H. Y., Wang, X. Y., Lu, S., Wang, R. S., Gao, X. L., & Wang, S. (2020). Turbulence-driven magnetic reconnection in the magnetosheath downstream of a Quasi-Parallel shock: A three-dimensional global hybrid simulation. *Geophysical Research Letters*, *47*(1), e2019GL085661. https://doi.org/10.1029/2019GL085661

Lu, S., Lin, Y., Lu, Q. M., Wang, X. Y., Wang, R. S., Huang, C., et al. (2015). Evolution of flux ropes in the magnetotail: A three-dimensional global hybrid simulation. *Physics of Plasmas*, *22*(5), 052901. https://doi.org/10.1063/1.4919615

Lu, S., Lu, Q. M., Lin, Y., Wang, X. Y., Ge, Y. S., Wang, R. S., et al. (2015). Dipolarization fronts as earthward propagating flux ropes: A three-dimensional global hybrid simulation. *Journal of Geophysical Research: Space*, *120*(8), 6286–6300. https://doi.org/10.1002/2015ja021213

Lu, S., Lu, Q. M., Wang, R. S., Pritchett, P. L., Hubbert, M., Qi, Y., et al. (2022). Electron-only reconnection as a transition from quiet current sheet to standard reconnection in Earth's Magnetotail: Particle-in-cell simulation and application to MMS data. *Geophysical Research Letters*, *49*(11), e2022GL098547. https://doi.org/10.1029/2022GL098547

Lu, S., Wang, R. S., Lu, Q. M., Angelopoulos, V., Nakamura, R., Artemyev, A. V., et al. (2020). Magnetotail reconnection onset caused by electron kinetics with a strong external driver. *Nature Communications*, *11*(1), 5049. https://doi.org/10.1038/s41467-020-18787-w

Newell, P. T., Sotirelis, T., Liou, K., Meng, C. I., & Rich, F. J. (2007). A nearly universal solar wind-magnetosphere coupling function inferred from 10 magnetospheric state variables. *Journal of Geophysical Research: Space*, *112*(A1), A01206. https://doi.org/10.1029/2006ja012015

Nykyri, K., Bengtson, M., Angelopoulos, V., Nishimura, Y., & Wing, S. (2019). Can enhanced flux loading by high-speed jets lead to a substorm? Multipoint detection of the Christmas day substorm onset at 08:17 UT, 2015. *Journal of Geophysical Research: Space*, *124*(6), 4314–4340. https://doi.org/10.1029/2018ja026357

Omidi, N., Blanco-Cano, X., Russell, C. T., & Karimabadi, H. (2004). Dipolar magnetospheres and their characterization as a function of magnetic moment. *Advances in Space Research*, *33*(11), 1996–2003. https://doi.org/10.1016/j.asr.2003.08.041

Palmroth, M., Laitinen, T. V., & Pulkkinen, T. I. (2006). Magnetopause energy and mass transfer: Results from a global MHD simulation. *Annales Geophysicae -Germany*, *24*(12), 3467–3480. https://doi.org/10.5194/angeo-24-3467-2006

Palmroth, M., Pulkkinen, T. I., Janhunen, P., & Wu, C. C. (2003). Stormtime energy transfer in global MHD simulation. *Journal of Geophysical Research: Space*, *108*(A1), 1048. https://doi.org/10.1029/2002ja009446

Pang, Y., Lin, Y., Deng, X. H., Wang, X. Y., & Tan, B. (2010). Three-dimensional hybrid simulation of magnetosheath reconnection under northward and southward interplanetary magnetic field. *Journal of Geophysical Research: Space*, *115*(A3), A03203. https://doi.org/10.1029/2009ja014415

Phan, T., Frey, H. U., Frey, S., Peticolas, L., Fuselier, S., Carlson, C., et al. (2003). Simultaneous cluster and IMAGE observations of cusp reconnection and auroral proton spot for northward IMF. *Geophysical Research Letters*, *30*(10), 1509. https://doi.org/10.1029/2003gl016885

Ren, J. Y., Guo, J., Lu, Q. M., Lu, S., Gao, X. L., Ma, J. Q., & Wang, R. S. (2024). Honeycomb-like magnetosheath structure formed by jets: Three-dimensional global hybrid simulations. *Geophysical Research Letters*, *51*(12), e2024GL109925. https://doi.org/10.1029/2024GL109925

Russell, C. T., & Elphic, R. C. (1978). Initial ISEE magnetometer results - Magnetopause observations. *Space Science Reviews*, *22*(6), 681–715. https://doi.org/10.1007/BF00212619

Shi, Q. Q., Zong, Q. G., Fu, S. Y., Dunlop, M. W., Pu, Z. Y., Parks, G. K., et al. (2013). Solar wind entry into the high-latitude terrestrial magnetosphere during geomagnetically quiet times. *Nature Communications*, *4*(1), 1466. https://doi.org/10.1038/ncomms2476

Slavin, J. A., Lepping, R. P., Gjerloev, J., Fairfield, D. H., Hesse, M., Owen, C. J., et al. (2003). Geotail observations of magnetic flux ropes in the plasma sheet. *Journal of Geophysical Research: Space*, *108*(A1), 1015. https://doi.org/10.1029/2002ja009557

Spencer, E., Srinivas, P., & Vadepu, S. K. (2019). Global energy dynamics during substorms on 9 March 2008 and 26 February 2008 using satellite observations and the WINDMI model. *Journal of Geophysical Research: Space*, *124*(3), 1698–1710. https://doi.org/10.1029/2018ja025582

Stern, D. P. (1984). Energetics of the magnetosphere. *Space Science Reviews*, *39*(1–2), 193–213. https://doi.org/10.1007/BF00173674

Sun, J. C., Ren, J. Y., Lu, Q. M., Zhang, B. C., & Yang, H. G. (2024). The transmission of Pc 3 waves from the foreshock into the Earth's magnetosphere: 3D global hybrid simulation. *Journal of Geophysical Research: Space*, *129*(10), e2024JA033007. https://doi.org/10.1029/2024ja033007

Suni, J., Palmroth, M., Turc, L., Battarbee, M., Johlander, Tarvus, A., Tarvus, V., et al. (2021). Connection between foreshock structures and the generation of magnetosheath jets: Vlasiator results. *Geophysical Research Letters*, *48*(20), e2021GL095655. https://doi.org/10.1029/2021GL095655

Tesema, F., Palmroth, M., Turc, L., Zhou, H., Cozzani, G., Alho, M., et al. (2024). Dayside Pc2 waves associated with flux transfer events in a 3D hybrid-Vlasov simulation. *Geophysical Research Letters*, *51*(3), e2023GL106756. https://doi.org/10.1029/2023GL106756

Torbert, R. B., Burch, J. L., Phan, T. D., Hesse, M., Argall, M. R., Shuster, J., et al. (2018). Electron-scale dynamics of the diffusion region during symmetric magnetic reconnection in space. *Science*, *362*(6421), 1391–1395. https://doi.org/10.1126/science.aat2998

Turc, L., Roberts, O. W., Verscharen, D., Dimmock, A. P., Kajdic, P., Palmroth, M., et al. (2023). Transmission of foreshock waves through Earth's bow shock. *Nature Physics*, *19*(1), 78–86. https://doi.org/10.1038/s41567-022-01837-z

Wang, S. M., Lu, S., Lu, Q. M., Wang, R. S., Ren, J. Y., Gao, X. L., & Guo, J. (2024). Origin of reconnecting current sheets in shocked turbulent plasma. *Science Advances*, *10*(33), eado4639. https://doi.org/10.1126/sciadv.ado4639

Wang, Z. W., Han, D. S., Chen, X. C., Shi, R., Teng, S. C., Zhang, J., et al. (2025). Observations of a throat aurora directly driven by magnetosheath high-speed jet. *Journal of Geophysical Research: Space*, *130*(1), e2024JA033276. https://doi.org/10.1029/2024ja033276

Wing, S., Johnson, J. R., Chaston, C. C., Echim, M., Escoubet, C. P., Lavraud, B., et al. (2014). Review of solar wind entry into and transport within the plasma sheet. *Space Science Reviews*, *184*(1–4), 33–86. https://doi.org/10.1007/s11214-014-0108-9

Xu, S. S., Liemohn, M. W., Dong, C. F., Mitchell, D. L., Bougher, S. W., & Ma, Y. J. (2016). Pressure and ion composition boundaries at Mars. *Journal of Geophysical Research: Space*, *121*(7), 6417–6429. https://doi.org/10.1002/2016ja022644

Yi, Y. Y., Zhou, M., Lin, Y., Pang, Y., Jin, R. Q., Song, L. J., & Deng, X. H. (2025). Global hybrid simulation of dayside magnetopause energy transport under purely southward interplanetary magnetic field. *Journal of Geophysical Research: Space*, *130*(1), e2024JA033045. https://doi.org/10.1029/2024JA033045

Zhang, H. X., Lu, J. Y., Wang, M., & Zhou, Y. (2024). Comparison of solar wind interaction with Mars and Earth: Energy transfer. *The Astrophysical Journal*, *968*(2), 84. https://doi.org/10.3847/1538-4357/ad463c

Zhang, Q. H., Zhang, Y. L., Wang, C., Oksavik, K., Lyons, L. R., Lockwood, M., et al. (2021). A space hurricane over the Earth's polar ionosphere. *Nature Communications*, *12*(1), 1207. https://doi.org/10.1038/s41467-021-21459-y